IEEE Access
Multidisciplinary | Rapid Review | Open Access Journal

Received April 4, 2019, accepted May 5, 2019, date of publication May 15, 2019, date of current version May 30, 2019.

Digital Object Identifier 10.1109/ACCESS.2019.2917153

An Adaptive CNNs Technology for Robust Iris Segmentation

YING CHEN, WENYUAN WANG, ZHUANG ZENG, AND YERONG WANG
School of Software, Nanchang Hangkong University, Nanchang 330063, China

Corresponding author: Wenyuan Wang (nchu_wwy@163.com)

This work was supported in part by the National Natural Science Foundation of China under Grant 61762067, Grant 61501217, Grant 61662049, and Grant 61867004, in part by the Natural Science Foundation of Jiangxi Province under Grant 20161BAB212034, and in part by the Jiangxi Province Education Department under Grant GJJ160692.

ABSTRACT Iris segmentation algorithms are of great significance in complete iris recognition systems, and directly affect the iris verification and recognition results. However, the conventional iris segmentation algorithms have poor adaptability and are not sufficiently robust when applied to noisy iris databases captured under unconstrained conditions. In addition, there are currently no large iris databases; thus, the iris segmentation algorithms cannot maximize the benefits of convolutional neural networks (CNNs). The main work of this paper is as follows: first, we propose an architecture based on CNNs combined with dense blocks for iris segmentation, referred to as a dense-fully convolutional network (DFCN), and adopt some popular optimizer methods, such as batch normalization (BN) and dropout. Second, because the public ground-truth masks of the CASIA-Interval-v4 and IITD iris databases do not include the labeled eyelash regions, we label these regions that occlude the iris regions using the Labelme software package. Finally, the promising results of experiments based on the CASIA-Interval-v4, IITD, and UBIRIS.V2 iris databases captured under different conditions reveal that the iris segmentation network proposed in this paper outperforms all of the conventional and most of the CNN-based iris segmentation algorithms with which we compared our algorithm's results in terms of various metrics, including the accuracy, precision, recall, f1 score, and nice1 and nice2 error scores, reflecting the robustness of our proposed network.

INDEX TERMS CNNs, dense block, dense-fully convolutional network, iris segmentation.

I. INTRODUCTION

Iris texture plays an important role in national defense and security because of its unique, stable, noncontact and anti-counterfeiting characteristics. A complete iris recognition system usually consists of the following steps: initially, iris images are obtained by an imaging device. Then, the iris regions of the eye images are located by iris segmentation algorithms. Next, iris features are extracted by feature extraction algorithms. Finally, the extracted iris features are used for iris verification or recognition. As shown in FIGURE 1, with the exception of the iris regions, the iris images consist of not only the iris regions but also other regions, i.e., pupil, eyelid, eyelashes and sclera [1]. The non-iris regions degrade the iris segmentation performance. Iris segmentation algorithms are designed to eliminate the effects of the non-iris regions and accurately segment the iris regions from the eye images. Iris segmentation algorithms are of great significance in iris recognition systems. The accuracy and robustness of the algorithms directly affect the subsequent iris extraction, verification and recognition stages [2]. Under ideal conditions—i.e., the iris regions are not occluded by the eyelids or eyelashes, the iris images are clear, and users are absolutely cooperative; thus, most existing iris segmentation algorithms can accurately segment the iris regions. However, under nonideal conditions, it is still challenging to design robust iris segmentation algorithms that accurately segment the iris regions despite the effects of eyelids, eyelashes, light, and user cooperation.

The associate editor coordinating the review of this manuscript and approving it for publication was Genny Tortora.

II. RELATED WORKS

Current iris segmentation algorithms consist of the following types:

1) Iris segmentation algorithms based on image gradients: Okokpujie *et al.* [4] proposed an iris segmentation algorithm that replaces integro-differential operators with the Hough

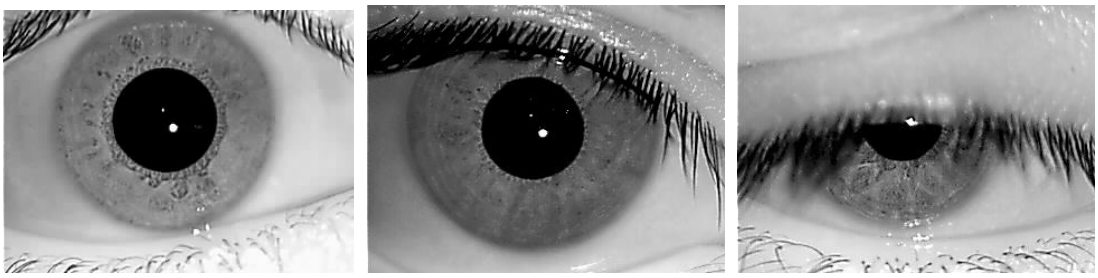

FIGURE 1. Samples of iris images under ideal and nonideal conditions. (a) Ideal iris images. (b) Iris images slightly occluded. (c) Iris images severely occluded.

transform, which increases the segmentation accuracy of the algorithm. Umer *et al.* [5] proposed a restricted Hough transform algorithm, which reduces the parameter search space of the traditional Hough transform algorithms, and the algorithm spends less time during the segmentation process and obtains higher accuracy. Roy *et al.* [7] proposed an improved algorithm based on the Daugman model, which can better eliminate noise, i.e., noise from eyelashes and eyelids, and more quickly segment the iris regions. Iris segmentation algorithms based on image gradients usually obtain good results under ideal conditions. However, under nonideal conditions, these algorithms are not sufficiently robust. On the one hand, such algorithms essentially locate the boundaries relying on the changes in the gray values at the edge or boundary of the iris. However, under nonideal conditions, high contrast among the eyelashes, light spots and iris exists, which makes it more difficult to accurately locate the iris boundaries. To solve these problems, it is necessary to eliminate the impact of eyelashes, eyelids and light spots before locating the iris boundaries. The iris segmentation framework proposed by Zhao *et al.* [9] is based on the total variation formula using L1 regularization, which robustly represses noise from the non-iris regions and increases the segmentation accuracy. On the other hand, the circularity of the iris boundaries also influences the segmentation accuracy. Some early iris segmentation algorithms achieved good results by assuming that the iris region is circular, but not all iris regions are circular. To accurately segment the iris regions, it is necessary to fill the iris boundaries. Uhl and Wild [10] first used an adaptive Hough transform algorithm to estimate the approximate position of the iris center. Then, a polar coordinate transformation was adopted to detect the first elliptical boundaries or the pupil boundaries. Finally, the elliptical polar coordinate transformation was adopted to find the second boundary according to the result of the first elliptical boundary. In summary, iris segmentation algorithms based on image gradients are not sufficiently robust in terms of the impact of eyelashes, eyelids, illumination and deformation. These algorithms need to preprocess iris images according to prior knowledge before or during the location of the iris boundaries, which undoubtedly increases the complexity of the algorithms. In addition, the correlated segmentation steps and the various thresholds that need to be determined both make the algorithm very complex.

2) Iris segmentation algorithms based on pixels: Radman *et al.* [11] adopted a circular Gabor filter to roughly estimate the pupil center and used the live-wire algorithm to find the upper and lower eyelid boundaries. Sahmoud and Abuhaiba [12] adopted the k-means algorithm to extract the expected area of the iris and then used the circular Hough transform algorithm to determine the iris radius and center. Hu *et al.* [8] improved the iris segmentation algorithms in several aspects. First, the segmentation results of different segmentation methods and models were combined to increase the segmentation accuracy. Then, histogram of gradient (HOG) features were used as the circle features of the iris regions. Finally, the support vector machine (SVM) method was used for classifying the iris and non-iris regions. Radman *et al.* [13] adopted a circular Gabor filter to classify the iris and non-iris regions. Radman *et al.* [14] adopted HOG as features and SVM was used to perform the automatic segmentation of iris. Barra *et al.* [6] adopted region of interest (ROI) detection and normalization via the Hough transform and iris clustering performed by means of simple linear iterative clustering (SLIC). Susitha *et al.* [41] detected the eyelids and pupil regions of eyes by performing parabolic and morphological operations. Similar to the iris segmentation algorithm based on image gradients, the iris segmentation algorithms based on pixels are also easily affected by eyelashes, eyelids, etc., which leads to a decrease in segmentation accuracy. These algorithms are also not adequately robust.

3) Iris segmentation algorithms based on CNNs: In recent years, CNNs have benefited from the excellent learning ability of convolution kernels and the data available in the era of big data; these frameworks have exhibited excellent performance in the fields of computer vision [15] [16]. CNNs also outperform traditional algorithms in the fields of semantic segmentation and instance segmentation. Fully convolutional networks (FCNs) [17] adopt pretrained models, such as AlexNet and VGGNet, for transfer learning and chang the fully connected layer structures in the CNNs for adopting transpose convolution to achieve the goal of semantic segmentation. Moreover, the segmentation accuracy was increased by 20%. Since then, SegNet [18], U-net [19]

TABLE 1. Comparisons of previous studies on iris segmentation.

Methods	Strengths	Weaknesses
Iris segmentation algorithms based on image gradients [4][5][7][9][10]	Fast and accurate segmentation in nonideal situations. No need for training parameters and large amounts of training data.	Finding the right threshold takes a considerable amount of time; not sufficiently robust on unconstrained capture conditons and on low-quality iris databases.
Iris segmentation algorithms based on pixels[6][8] [11][12] [13][14][41]	Better performance is obtained by removing closed eye, eyelash and eyelid influences and there is no need for a large number of samples.	A separate method for eyelash, pupil and iris detection is time consuming and not sufficiently robust under unconstrained capture conditions and on low-quality iris databases..
Iris segmentation algorithms based on CNNs [23] [24][42][43][45]	Better accuracy due to CNNs and a lower error than conventional methods for nonideal cases.	To improve the performance of CNN, data augmentation and preprocessing methods for training datasets should be adopted. Moreover, most present methods based on CNNs do not maximize the benefits of deep CNNs. Methods based on CNNs need additional training time and training parameters.
Our proposed method	(1) No data augmentation methods and preprocessing methods are adopted. (2) Promising results are obtained due to the dense connection.	Dense connections are more time consuming; moreover, comparing to some conventional iris segmentation methods, our proposed method requires more training parameters.

and other algorithms have continuously improved the network structures or convolution methods for improving the performance. In different fields, such as medical and road condition image processing, these CNNs have shown the advantages relative to traditional algorithms. In the field of iris recognition, Marra *et al.* [20] adopted CNNs to classify iris images acquired by different image devices. Ribeiro *et al.* [21] proposed two deep learning structures for iris recognition: stacked auto-encoders (SAEs) and CNNs. Furthermore, the results of experiments reveal the superiority of deep learning structures. Al-Waisy *et al.* [22] proposed a shallow CNN for iris recognition, in which the features of the iris and face are combined to obtain excellent results. However, in the field of iris segmentation, only a few articles have proposed iris segmentation algorithms based on CNNs. Jalilian and Uhl [23] proposed three iris segmentation network structures based on FCNs and named them fully convolutional encoder–decoder networks (FCEDNs), and the results of their experiments show that FCEDNs are superior to all of the traditional algorithms. Liu *et al.* [24] proposed two CNNs: hierarchical convolutional neural networks (HCNNs) and multi-scale fully convolutional networks (MFCNs) to solve the problem of the performance degradation of traditional iris segmentation algorithms under nonideal conditions. Moreover, MFCNs are more robust than HCCNs, and the segmentation accuracy of MFCNs increased by 25.62% and 13.24% compared with that of HCCNs on the adopted datasets. Shabab *et al.* [42] designed optimized deep neural networks for iris segmentation under unconstrained capture conditions, which obtained promising performance on lower quality datasets. Arsalan *et al.* [43] proposed a segmentation network that uses the complete image without prior preprocessing and named it IrisDenseNet, which can determine the true iris boundary even with inferior-quality images by using improved information gradient flow between the dense blocks. Arsalan *et al.* [44] proposed iris segmentation models based on the residual skip connection.

Based on the analysis of the above literature, on the one hand, traditional iris segmentation algorithms are not sufficiently adaptive and robust under nonideal conditions. However, current iris segmentation algorithms based on CNNs have not yet fully taken advantage of deep CNNs. Therefore, this paper proposes a robust architecture based on CNNs combined with dense blocks [25], termed dense-fully convolutional network (DFCN), which adaptively segments out the iris regions of iris images. Comparative analyses of our proposed method with other iris segmentation methods are summarized in TABLE 1.

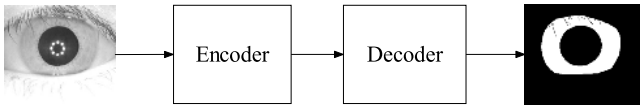

FIGURE 2. The FCN architecture.

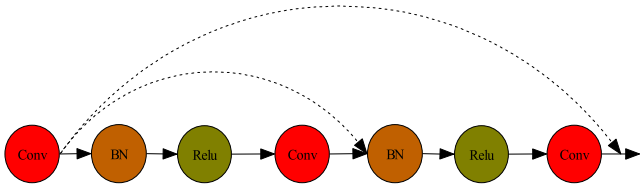

FIGURE 3. Dense block composed of 3 convolutional layers.

The remainder of this paper is organized as follows: Section 3 describes in detail the proposed adaptive DFCN and the training strategies of the structure model. The details of the public iris image databases employed and corresponding ground-truth masks are represented in Section 4, and the evaluation metrics are also described. The experimental results, comparisons with state-of-the-art methods, and a discussion are presented in Section 5. Section 6 summarizes this study.

III. THE PROPOSED ARCHITECTURE FOR IRIS SEGMENTATION

A. OVERVIEW OF FCNS AND DENSE BLOCKS

As shown in FIGURE 2, FCNs include an encoder and a decoder. In the encoder, image features are extracted, and downsampling operations are performed. The encoder is a pretrained AlexNet or VGGNet in most FCNs, which extracts features of the adopted databases by means of transfer learning. In the decoder, upsampling operations are adopted for the features by means of transpose convolution, and the output prediction masks are obtained. FCNs change the structures of conventional CNNs. Conventional CNNs consist of only an encoder, which outputs the distribution of probabilities in the fully connected layers. However, FCNs change the fully connected layers to 1×1-sized spatial structures, aiming to obtain prediction masks from the decoder via transpose convolution.

Deep CNNs extract more discriminative features than shallow CNNs because the former have a superior learning ability. However, deep CNN training has limits for iris segmentation. First, there are no large iris databases at present for training deep CNNs, and the small iris databases lead to overfitting. In addition, gradient vanishing degrades the accuracy for deep CNNs. Therefore, dense blocks are adopted as the fundamental structure of the proposed architecture in this paper.

As demonstrated in FIGURE 3, the top convolutional layers connect the later convolutional layers, and each convolutional layer is followed by the rectified linear unit (ReLU) layers and batch normalization (BN) layers. Assuming there are L convolutional layers, the conventional CNNs have L connections, but there are connections in the CNNs based on the dense block. The dense blocks alleviate the overfitting and gradient vanishing effectively, which add the larger feature value of the bottom layers to the small feature value of the top layers.

B. THE PROPOSED ARCHITECTURE AND TRAINING STRATEGIES

An FCN architecture based on dense blocks is proposed in this paper. This architecture is named DFCN.

As shown in FIGURE 4, the encoder of DFCN is given in the left half and is named the Dense-encoder, and the decoder of DFCN is given in the right half and named the Dense-decoder. The convolutional layers are labeled to 'Conv', and the dense blocks are labeled to 'DB'. The pooling layers are labeled to 'PL'. The transpose convolutional layers are labeled to 'Conv_t'. The processing layers are labeled to 'Pro_L'. The details of DFCN are summarized in TABLE 2.

As can be observed from TABLE 2, in the Dense-encoder, the input images are first convolved by Conv1, which consists of 64 convolutional kernels with a 3×3 size and stride 1. Conv1 is followed by 5 dense blocks, which are named Denseblock1, Denseblock2, Denseblock3, Denseblock4 and Denseblock5. The dense blocks are composed of two 3×3 convolutional layers with 48 kernels and a step size of 1, and 96 channels of feature maps are added through a dense block. The convolutional layers of the dense blocks are followed by the BN layers and ReLU layers. Pooling layers follow after each dense block and are referred to as Pooling layer 1, Pooling layer 2, Pooling layer 3, Pooling layer 4 and Pooling layers 5. The pooling layers perform the average-pooling operation over a 2×2 window with stride 2. The last pooling layer is followed by Conv6, Conv7 and the score layers. Conv6 is composed of 4096 kernels with 7×7 size and step 1. Conv7 is composed of 4096 kernels with 1×1 size and step 1. The score layer is composed of n kernels with 1×1 size and step 1, where n is 2 in this paper, namely, the iris pixels and non-iris pixels. In the Dense-decoder, the n channel feature maps obtained from the Dense-encoder are sampled by the transpose layers Conv_t1, Conv_t2, Conv_t3, Conv_t4 and Conv_t5, and the output prediction masks are obtained. The pixel values of the prediction masks are 0 or 1, where 0 denotes the non-iris pixels and 1 represents the iris pixels. Except for Conv_t5, all transpose convolutional layers fuse the same size output of the pooling layers in the Dense-encoder by adding the pixel values of the feature maps, i.e., Fuse1, Fuse2, Fuse3 and Fuse4, with 3×3 kernels and step 2. Additionally, all fuse layers are followed by processing layers, referred to as Pro_L1, Pro_L2, Pro_L3 and Pro_L4 in FIGURE 4. The process layers are composed of two successive convolutional layers. The first one consists of double numbers of previous layers kernels with 3×3 size and step 1. The second one consists of half numbers of previous layers kernels with 1×1 size and step 1. All convolutional kernels are padded with zeros.

At the end of the Dense-decoder, the cross entropy function is adopted as the cost function. The cost function J is

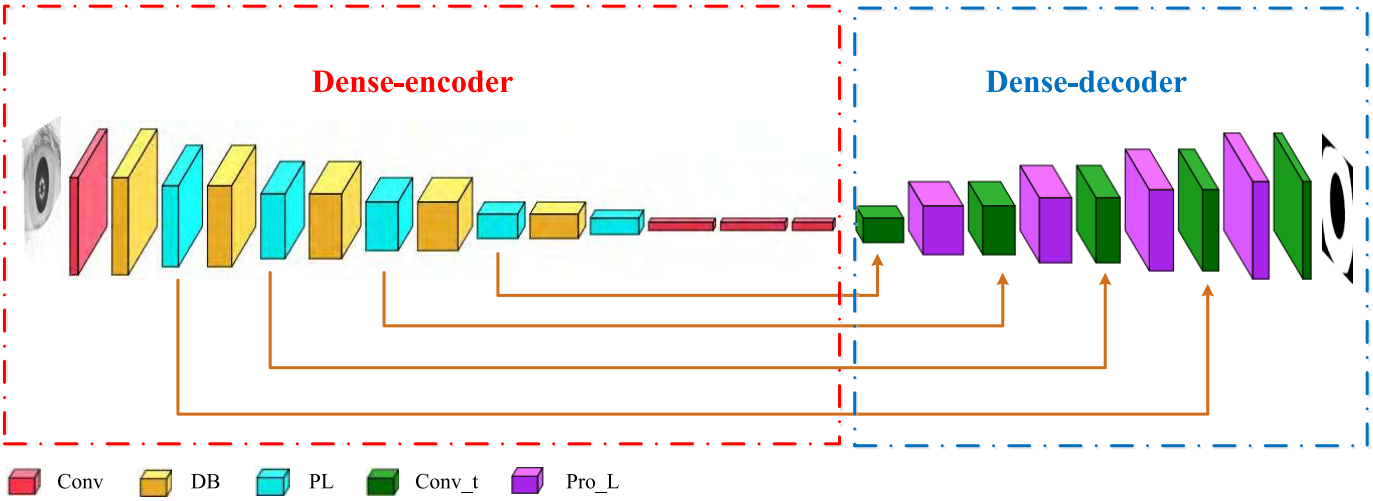

FIGURE 4. The DFCN architecture.

as follows, where, $\tilde{f}_j(z)$ denotes the desired label probabilities of the training image and $f_j(z)$ denotes the actual network output:

$$J(\theta) = \frac{1}{m}\sum_{i=1}^{m}\sum_{j=1}^{c}\tilde{f}_j(z)\log\left[f_j(z)\right] \tag{1}$$

For optimization, we adopted the mini-batch Adam algorithm [29] to minimize the cost function. The iris images are composed of mostly non-iris regions and a few iris regions, which lead to the adoption of the standard stochastic gradient descent (SGD) algorithm, which obtains many non-iris features and ignores the iris features. That is, the iris features are sparse, and the non-iris features are common. However, the Adam algorithm increases the learning rate for sparse data and decreases it for common data, and it updates quickly for sparse features and slowly for common features. The Adam algorithm computes the learning rate η for every parameter θ_i at each time step t based on the previous gradients of the same parameter as follows:

$$\widehat{m}_t = \frac{m_t}{1-\mu^t} \tag{2}$$

$$\widehat{n}_t = \frac{n_t}{1-v^t} \tag{3}$$

$$\theta_i^{t+1} = \theta_i^{t+1} - \frac{\widehat{m}_t}{\sqrt{\widehat{n}_t + \varepsilon}} * \eta \tag{4}$$

where $m_t = \mu^* m_{t-1} + (1-\mu)^* g_t$ is the estimate of the first-order moment, $n_t = v^* n_{t-1} + (1-v)^* g_t^2$ is the estimate of second-order moment, and $g_t = \nabla_\theta J(\theta)$ denotes the gradient of the cost function. In addition, μ and v are the exponential decay rates of m_t and n_t, respectively, which are assigned a constant value, and ε is a small constant to avoid division by zero.

Initially, we set the learning rate to 0.001. Moreover, the maximum iterative step is set to 30000, and the batch size is set to 2. The learning rate decreases by a factor of 10 every 10000 steps. The weights of all convolutional kernels are initialized as a truncated normal distribution with a standard deviation of 0.01, and the bias of all convolutional layers is 0. The values of μ and v of the mini-batch Adam algorithm are set to 0.9 and 0.99, respectively. Finally, the saved model in the 30000 steps is used for prediction. Notably, pretrained models are not adopted for the Dense-decoder. Importantly, we train the DFCN from scratch.

IV. EXPERIMENTAL CONFIGURATION

A. DESCRIPTION OF THE IRIS IMAGE DATABASE

To evaluate our proposed architecture, we adopted three public iris databases collected under different conditions: the CASIA-Interval-V4 [26], IITD [27] and UBIRIS.V2 [31] iris databases. The CASIA-Interval-V4 iris database is provided by the Institute of Automation, Chinese Academy of Science and which includes 2639 images of 249 different subjects. All images from the CASIA-Interval-V4 iris database were captured with a self-developed close-up iris camera. The IITD iris database is provided by the IIT Delhi, New Delhi, India and which contains a total of 2240 images of 224 different subjects. All images of the IITD iris database were captured using three different cameras: JIRIS, JPC1000, and digital complementary metal–oxide–semiconductor (CMOS) cameras, and each subject included 5 left iris images and 5 right iris images. The UBIRIS.V2 iris database, provided by Department of Computer Science, University of Beira Interior, has 11102 images from 522 irises of 261 different subjects taken in an unconstrained environment. All images in the UBIRIS.V2 iris database were captured with a Canon EOS 5D camera. Moreover, these images were captured under unconstrained conditions, i.e., on-the-move, off-axis, occluded, with reflections and glasses, at distance and under several realistic lighting conditions. Notably, the CASIA-Interval-V4 and IITD iris databases were taken under near-infrared illumination (NIR);

TABLE 2. The architecture details of DFCN.

Name	Type/Kernel/Stride/No. of kernel		Output size	Numbers of parameters
Dense-encoder				
Input	——		300×400×3	——
Conv1	Convolution/3×3/1/64		300×400×64	1.7K
Dense block 1	Batch Normalization, ReLU, Convolution/3×3/1/48 concatenation	X 2	300×400×112 300×400×160	161K
Pooling layer 1	Average-pooling/2×2/2/——		150×200×160	——
Dense block 2	Batch Normalization, ReLU, Convolution/3×3/1/48 concatenation	X 2	150×200×208 150×200×256	479K
Pooling layer 2	Average-pooling/2×2/2/——		75×100×256	——
Dense block 3	Batch Normalization, ReLU, Convolution/3×3/1/48 concatenation	X 2	75×100×304 75×100×352	963K
Pooling layer 3	Average-pooling/2×2/2/ ——		38×50×352	——
Dense block 4	Batch Normalization, ReLU, Convolution/3×3/1/48 concatenation	X 2	38×50×400 38×50×448	1612K
Pooling layer 4	Average-pooling/2×2/2/——		19×25×448	——
Dense block 5	Batch Normalization, ReLU, Convolution/3×3/1/48 concatenation	X 2	10×13×496 10×13×544	2428K
Pooling layer 5	Average-pooling/2×2/2/——		10×13×544	——
Conv6	Convolution/7×7/1/4096		10×13×4096	109182K
Dropout1	Dropout (50%)		——	——
Conv7	Convolution/1×1/1/4096		10×13×4096	16777K
Dropout2	Dropout (50%)		——	——
Score	Convolution/1×1/1/ Class numbers		10×13×Class numbers	——
Dense-decoder				
Conv_t1	De_Convolution/3×3/2/448		19×25×448	8K
Fuse1	Fusion(+Pooling layer 4)		19×25×448	——
Process layer 1	Batch Normalization, ReLU, Convolution/3×3/1/896		19×25x896	3612K
	Batch Normalization, ReLU, Convolution/1×1/1/448		19x25x448	401K
Conv_t2	De_Convolution/3×3/2/352		38×50×352	1419K
Fuse2	Fusion(+Pooling layer 3)		38×50×352	——
Process layer 2	Batch Normalization, ReLU, Convolution/3×3/1/704		38×50×704	2230K
	Batch Normalization, ReLU, Convolution/1×1/1/352		38×50×352	247K
Conv_t3	De_Convolution/3×3/2/256		75×100×256	811K
Fuse3	Fusion(+Pooling layer 2)		75×100×256	——
Process layer 3	Batch Normalization, ReLU, Convolution/3×3/1/512		75×100×512	1179K
	Batch Normalization, ReLU, Convolution/1×1/1/256		75×100×256	131K
Conv_t4	De_Convolution/3×3/2		150×200×160	368K
Fuse4	Fusion(+Pooling layer 1)		150×200×160	——
Process layer 4	Batch Normalization, ReLU, Convolution/3×3/1/320		150×200×320	460K
	Batch Normalization, ReLU, Convolution/1×1/1/160		150×200×160	51K
Conv_t5	De_Convolution/3×3/2/2		300×400×Class numbers	——
prediction	——		300×400×1	——

TABLE 3. The characteristics of the adopted iris image databases.

Property	CASIA-Iris-V4	IITD	UBIRIS.V2
Number of classes	249	224	50
Number of images	2639	2240	2250
Samples per subject	——	5 left iris images and 5 right iris images	——
Image size	320×280 pixels	320×240 pixels	400×300 pixels
Image format	JPEG	BMP	TIFF
Illumination environments	NIR	NIR	Visible

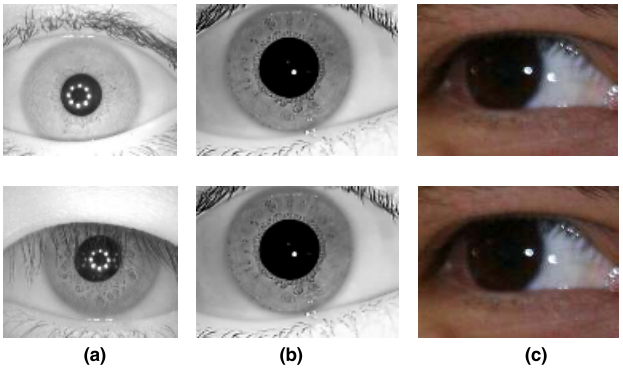

FIGURE 5. Image samples from the adopted iris databases. (a) CASIA-Interval-V4. (b) IITD. (c) UBIRIS.V2.

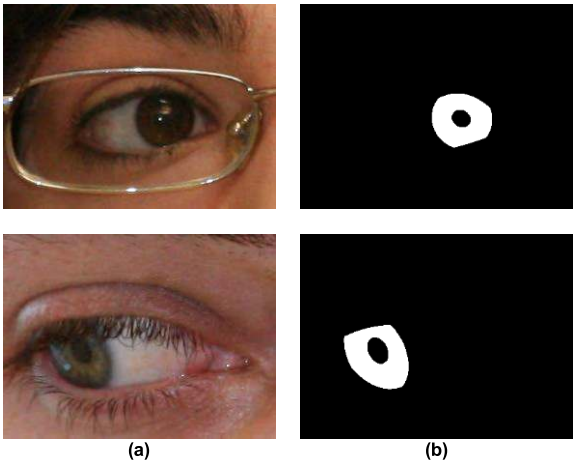

FIGURE 6. Samples of the UBIRIS.v2 ground-truth masks. (a) Original iris images. (b) Ground-truth masks.

nevertheless, the UBIRIS.V2 iris database was captured under visible illumination. Importantly, we did not adopt any data augmentation methods to enhance the adopted iris databases. Moreover, all images from the CASIA-Interval-V4 and IITD iris databases were adopted for training and testing. 2250 iris images from UBIRIS.V2 iris databases were adopted for training and testing. The basic characteristics of these three databases are summarized in TABLE 3.

As shown in FIGURE 5, on the one hand, the images of the CASIA-Interval-V4 and IITD databases consist of complete iris regions and iris regions occluded by eyelashes, etc. On the other hand, the images from the CASIA-Interval-V4 database were captured from individuals of Chinese origin, and the eyelashes are relatively fine and sparse. Nevertheless, the images from the IITD database were captured from individuals of Indian origin people with relatively thick eyelashes. Such problems make designing an iris segmentation algorithm more difficult. In addition, most iris images of the UBIRIS.V2 iris database were captured under unconstrained environments. As shown in FIGURE 5, the two iris images of UBIRIS.V2 were captured on-the-move and with less illumination. Therefore, iris segmentation tasks using the UBIRIS.V2 iris database are challenging.

The ground-truth masks of the UBIRIS.V2 iris database are provided by WaveLab of the University of Salzburg and are named Irisseg-ep [30]. However, the UBIRIS.V2 ground-truth masks of Irisseg-ep are not complete; the database contains only 2250 ground-truth masks from 50 subjects. FIGURE 6 shows some samples of the ground-truth masks of UBIRIS.V2.

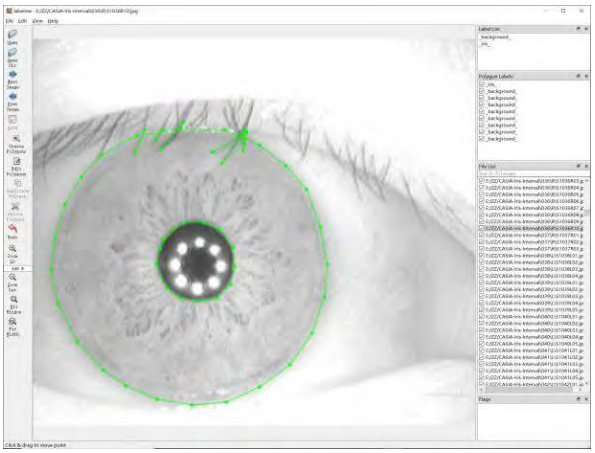

FIGURE 7. The process of labeling using Labelme.

Nevertheless, two different corresponding ground-truth masks of CASIA-Interval-V4 and IITD are adopted in this paper. The first ground-truth masks are provided by Irisseg-ep, which includes the corresponding ground-truth masks of CASIA-Interval-V4 and IITD. However, the noise, such as eyelashes, was not labeled in Irisseg-ep. To evaluate DFCN robustness, we adopt Labelme [28] for labeling the iris regions and the noise regions occluding the iris regions. FIGURE 7 shows the process of labeling. First, we label the outer ring of iris as '_iris_'. Second, the inner ring of iris is labeled as '_background_'. Finally, the eyelashes occluding the iris area are labeled as '_background_'. The other regions,

TABLE 4. The characteristics of the adopted iris image databases after splitting.

Property	CASIA-Iris-V4	IITD	UBIRIS.V2
The number of training sets	2111	1792	1800
The number of test sets	528	448	450
Image size	320×280 pixels	320×240 pixels	400×300 pixels

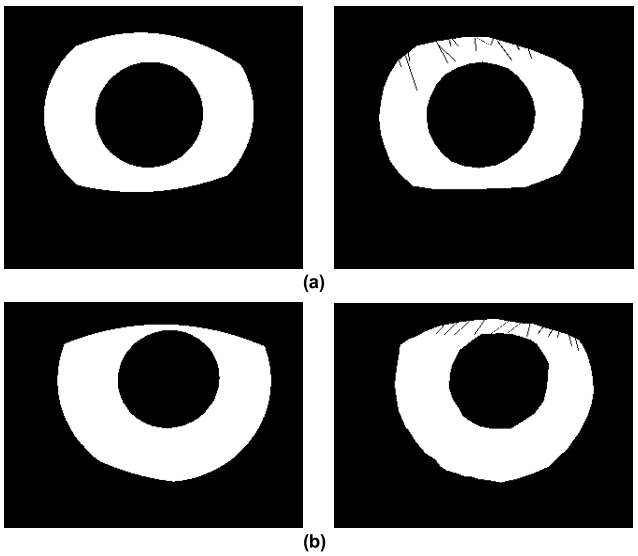

FIGURE 8. Samples of two different ground-truth masks. (a) Two different ground-truth masks of CASIA-Interval-V4. (b) Two different ground-truth masks of IITD.

i.e., sclera and eyelids, in the images are labeled as '_background_'. For the UBIRIS.V2 iris database, it is very difficult to label the noise regions due to the low quality of iris images. Therefore, we did not label the UBIRIS.V2 iris database.

FIGURE 8 shows the samples of two different ground-truth masks. The first row demonstrates the samples of public ground-truth masks, and the second row demonstrates corresponding samples whose eyelashes are labeled. It is more difficult to accurately segment iris regions on the ground-truth masks whose noise regions are labeled.

In all of our experiments, the iris datasets are divided into two parts, training sets and test sets, which are split according to a ratio of 8:2. As presented in TABLE 4, the training set of CASIA-Interval-V4 contains 2111 iris images, and the test set contains 528 iris images. The training set of IITD consists of 1792 iris images, and the test set consists of 448 iris images. The training set of UBIRIS.V2 includes 1800 iris images, and the test set includes 450 iris images. We adopt the open-source deep learning framework TensorFlow [45] to implement our architecture. Furthermore, our experiments were performed on an Inter Core i9-7900x CPU with 32 GB memory and an NVIDIA 1080ti GPU with 11 GB memory.

B. METRICS AND MEASUREMENTS FOR EXPERIMENTS

To assess the performance of DFCN and compare it with that of other iris segmentation algorithms, we adopt a variety of evaluation metrics. In this context, we consider the nice1 segmentation error score, which is widely accepted for the evaluation of iris segmentation. The nice1 segmentation error score calculates the average proportion of corresponding disagreeing pixels by performing the logical exclusive-or operator over all images of the test sets as follows:

$$\text{nice1} = \frac{1}{\text{n} \times \text{c} \times \text{r}} \sum_{\text{c}'} \sum_{\text{r}'} \text{O}(\text{c}', \text{r}') \oplus \text{C}(\text{c}', \text{r}') \tag{5}$$

where n is the number of test sets, c and r denote the width and height of test iris images, and $O(c', r')$ and $C(c', r')$ are pixels of the prediction and the ground-truth masks, respectively. The values of nice1 are bounded in the [0,1] interval, and 1 represents the worst value, while 0 is the optimal value. Moreover, to solve the disproportion between the prior probabilities of iris and non-iris pixels in the images, the type-I and type-II error score nice2 is calculated as follows:

$$\text{FPR} = \frac{\text{FP}}{\text{FP} + \text{TN}} \tag{6}$$

$$\text{FNR} = \frac{\text{FN}}{\text{TP} + \text{FN}} \tag{7}$$

$$\text{nice2} = \frac{(\text{FPR} + \text{FNR})}{2} \tag{8}$$

where *FP (false positive)* and *FN (false negative)* denote the misclassification number of non-iris pixels and iris pixels in test images, respectively. *TP (true positive)* and *TN (true negative)* denote the recognition number of iris pixels and non-iris pixels in test images, respectively. The values of nice2 are bounded in the [0,1] interval, and 1 represents the worst value, while 0 is the optimal value. Moreover, the accuracy, precision, recall and f1 score are also adopted for evaluation. The accuracy represents the correct segmentation pixels and is calculated as follows:

$$\text{acc} = \frac{\text{TP} + \text{TN}}{\text{TP} + \text{FN} + \text{FP} + \text{TN}} \times 100\% \tag{9}$$

The precision gives the average proportion of the correct classification number of iris pixels in all pixels that are classified as iris pixels. The precision is calculated as follows:

$$\text{p} = \frac{\text{TP}}{\text{TP} + \text{FP}} \tag{10}$$

The recall denotes the average proportion of the correct classification number of iris pixels in all pixels that belong to iris pixels. The recall is calculated as follows:

$$\text{r} = \frac{\text{TP}}{\text{TP} + \text{FN}} \tag{11}$$

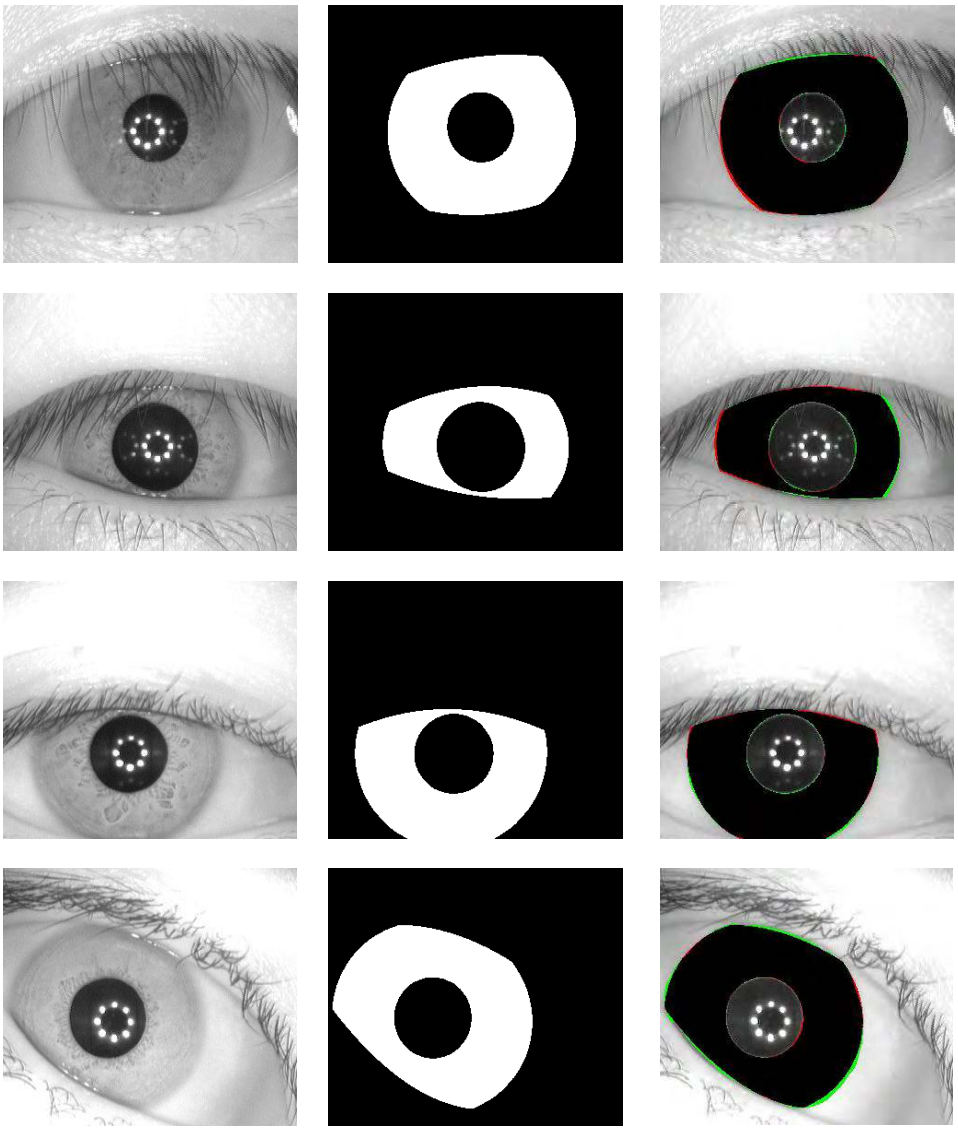

FIGURE 9. Some segmentation results of the CASIA-Iris-V4 iris database. (a) Original iris images. (b) Ground truth masks. (c) Segmentation results.

The F1 score is the harmonic mean of the precision and the recall and is calculated as follows:

$$\mathrm{f1} = \frac{2\mathrm{rp}}{\mathrm{r}+\mathrm{p}} \tag{12}$$

The accuracy, precision, recall and f1 score are bounded in the interval [1,0]. Different from nice1 and nice2, 0 represents the worst values, while 1 represents the optimal values.

V. COMPARISONS WITH OTHER METHODS AND DISCUSSION

To reflect the effectiveness and robustness of our proposed architecture, we compare the experimental results with other iris segmentation algorithms. First, we compare the results with some conventional iris segmentation algorithms. Moreover, comparisons with the iris segmentation algorithms based on CNNs are given in the section. Finally, the different results in different ground-truth masks are summarized. Some segmentation results of adopted the three iris databases are shown in FIGURE 9, FIGURE 10 and FIGURE 11.

FIGURE 9(a), FIGURE 10(a) and FIGURE 11(a) show the original iris images of the adopted iris databases, and FIGURE 9(b), FIGURE 10(b) and FIGURE 11(b) show the corresponding ground-truth masks. Additionally, FIGURE 9(c), FIGURE 10(c) and FIGURE 11(c) show the segmentation results where the false positive and negative errors are presented as green and red, respectively, and the true positive case is shown as black.

A. THE COMPARISONS OF CONVENTIONAL IRIS SEGMENTATION ALGORITHMS AND DFCN

A series of conventional iris segmentation algorithms are compared with our proposed architecture: A restricted Hough

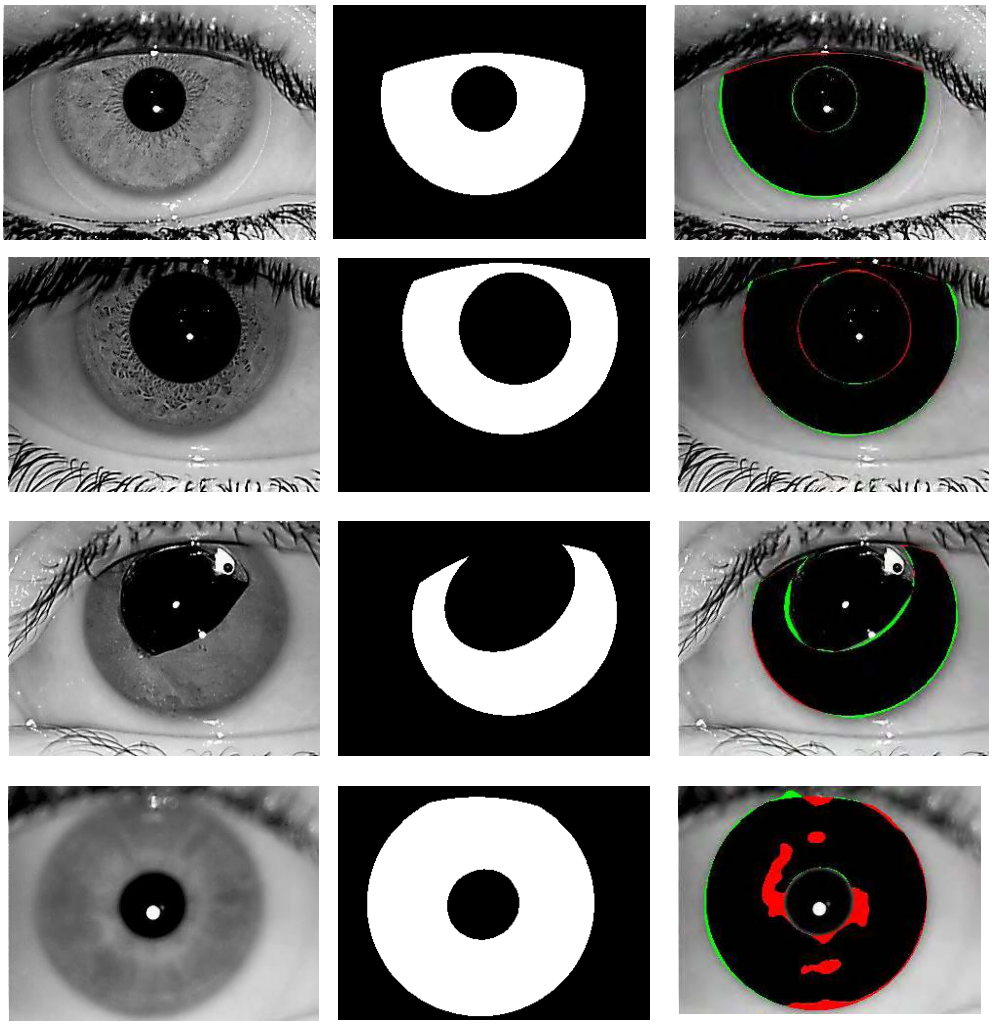

FIGURE 10. Some segmentation results of the IITD iris database. (a) Original iris images. (b) Ground truth masks. (c) Segmentation results.

transform algorithm was adopted by Umer et al. for locating the boundaries of iris [32]. Wild *et al.* [33] combined different iris segmentation algorithms to improve the segmentation accuracy. An integro-differential constellation followed by a curvature fitting model to find the iris area was proposed by Tan *et al.* [34]. Gangwar *et al.* [35] adopted a coarse-to-fine strategy to localize different iris boundaries. Zhao *et al.* [9] utilized the total variation (TV) model to overcome the problem of low contrast and noise interference in eye socket images. In addition, comparisons with state-of-the-art methods such as the generalized structure tensor (GST) [36], contrast-adjusted Hough transform (CAHT) [37], Osiris [38], iterative Fourier-based pulling and pushing (IFPP) [39] and Masek [40] methods are also given. The details of the comparisons are summarized in TABLE 5.

For the CASIA-Interval-V4 iris database, it can be observed from TABLE 5 that the accuracy of DFCN is 99.05%, which is greater than that of the other conventional iris segmentation algorithms. The precision, recall and f1 score with values of 0.9827, 0.9829 and 0.9828 are greater than those of conventional iris segmentation algorithms. Moreover, the values of the nice1 and nice2 error scores are less than those of conventional iris segmentation algorithms, which are 0.0094 and 0.0118, respectively. For the IITD iris database, TABLE 5 indicates that the accuracy of DFCN is 98.84%, which is also greater than that of the other conventional iris segmentation algorithms. The precision, recall and f1 score with values of 0.9818, 0.9806 and 0.9812 are greater than those of conventional iris segmentation algorithms. In addition, the values of the nice1 and nice2 error scores are less than those of conventional iris segmentation algorithms, which are 0.0115 and 0.0137, respectively. For the UBIRIS.V2 iris database, the highest accuracy of 99.47% is obtained; in addition, the precision, recall and f1 score with values of 0.9592, 0.9620 and 0.9606, respectively, are greater than those of conventional iris segmentation algorithms.

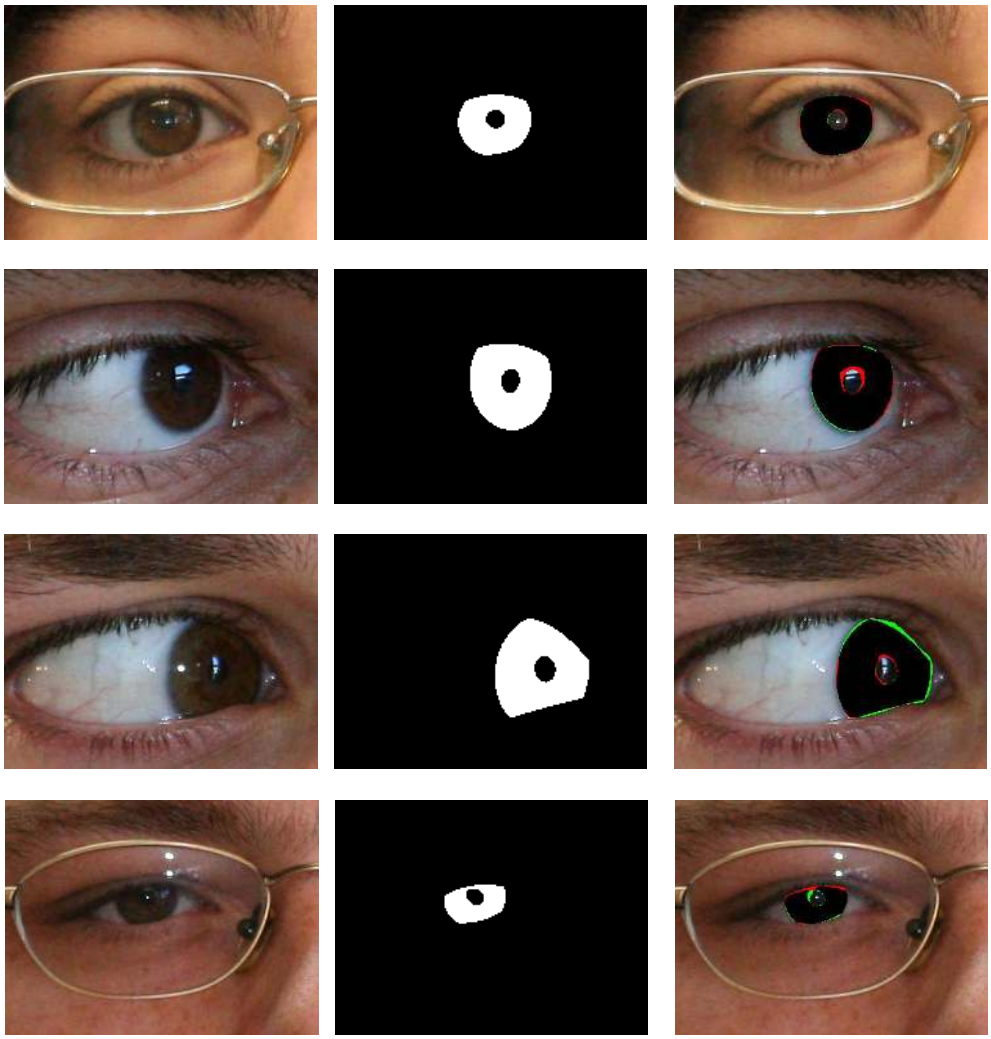

FIGURE 11. Some segmentation results of the UBIRIS.V2 iris database. (a) Original iris images. (b) Ground truth masks. (c) Segmentation results.

On the one hand, the results demonstrate that the effectiveness of DFCN is better than the conventional iris segmentation algorithms on all metrics. On the other hand, we did not adjust any of the parameters on different iris databases, reflecting the adaptability of DFCN. In addition, the types of parameters used in training DFCN are far less than those of conventional iris segmentation algorithms. Moreover, there are many complex steps in conventional iris segmentation algorithms.

B. THE COMPARISONS OF IRIS SEGMENTATION ALGORITHMS BASED ON CNNS AND DFCN

A comparison of iris segmentation algorithms based on CNNs and DFCN is presented in this section. Jalilian and Uhl [23] proposed three CNN architectures for iris segmentation, which are named FCEDNs-Original, FCEDNs-Basic and FCEDNs-Bayesian-Basic. The encoder of FCEDNs-Original contains 5 blocks and 44 layers, and the decoder contains 5 corresponding blocks and 44 layers. The FCEDNs-Original consists of 88 layers. Some convolutional layers of FCEDNs-Basic are removed; thus, the encoder and decoder of FCEDNs-Basic both contain 16 layers. FCEDNs-Basic consists of 32 layers. Based on FCEDNs-Basic, the encoder of FCEDNs-Bayesian-Basic is added to two dropout layers on the end, and the decoder of FCEDNs-Bayesian-Basic is added to the two corresponding dropout layers. Thus, FCEDNs-Bayesian-Basic consists of 36 layers. The MFCN and HCNN models proposed by Liu *et al.* [24] consist of 22 layers and have mainly been used on low-quality iris images. Different results were reported by Shabab *et al.* [42], which were obtained from different models: FCDNN-original, FCDNN-Segnet and FCDNN-tuning. The best result was obtained from FCDNN-tuning, which was initially trained on NIR images and later tuned on additional datasets derived from visible images. The results are summarized in TABLE 6.

TABLE 5. Comparison of DFCN with conventional algorithms on the three iris databases.

Database	Approach	Acc(%)	P	R	F1	Nice1	Nice2
CASIA-Interval-V4	Uhl et al. [10]	74%	—	—	0.8949	0.0608	0.0842
	Umer et al. [32]	95.87%	—	—	—	—	—
	Wild et al. [33]	98.13%	—	—	—	—	—
	Gangwar et al. [35]	—	0.9215	0.9426	0.9310	—	—
	GST[36]	—	0.8991	0.8519	0.8616	—	—
	CAHT[37]	—	0.8289	0.9768	0.8927	0.1161	0.1470
	Osiris[38]	—	0.9303	0.9732	0.8985	0.0565	0.0673
	IFPP[39]	—	0.8350	0.9174	0.8686	0.1532	0.2372
	Masek[40]	—	0.8900	0.8846	0.8830	—	—
	DFCN	**99.05%**	**0.9827**	**0.9829**	**0.9828**	**0.0094**	**0.0118**
IITD	Uhl et al. [10]	—	—	—	—	0.1377	0.1762
	Umer et al. [32]	98.48%	—	—	—	—	—
	Wild et al. [33]	97.60%	—	—	—	—	—
	Gangwar et al. [35]	—	0.9370	0.9533	0.9437	—	—
	GST[36]	—	0.8586	0.9006	0.8660	—	—
	CAHT[37]	—	0.7887	0.9660	0.8628	0.1138	0.1560
	Osiris[38]	—	0.9101	0.9406	0.9223	0.0555	0.0757
	IFPP[39]	—	0.7976	0.9392	0.8583	0.1142	0.1508
	Masek[40]	—	0.9045	0.8283	0.8530	—	—
	DFCN	**98.84%**	**0.9818**	**0.9806**	**0.9812**	**0.0115**	**0.0137**
UBIRIS.v2	Radman et al. [14]	98.28%	—	—	—	—	—
	Zhao et al. [44]	98.79%	—	—	—	—	—
	Tan et al. [34]	98.69%	—	—	—	—	—
	GST[36]	—	0.3931	0.4259	0.3993	—	—
	CAHT[37]	—	0.1139	0.1802	0.1225	—	—
	Osiris[38]	—	0.1729	0.2646	0.1865	—	—
	IFPP[39]	—	0.2371	0.4438	0.2852	—	—
	Uhl et al. [10]	—	0.2276	0.2740	0.2368	—	—
	DFCN	**99.47%**	**0.9592**	**0.9620**	**0.9606**	**0.0052**	**0.0204**

From TABLE 6, in terms of all metrics, the results of DFCN outperform most of the other methods based on CNNs. On the CASIA-Interval-V4 iris database, the highest accuracy of 99.05% is obtained from DFCN. In addition, the highest precision and F1 scores of 0.9827 and 0.9828 and the lowest nice1 and nice2 errors of 0.0094 and 0.0118 are obtained from DFCN. However, the recall of 0.9829 obtained from DFCN is less than the value of 0.9910 obtained from the FRED-Net [44]. Similarly, on the IITD iris database, the highest accuracy of 98.84% is obtained from DFCN. Besides, the highest precision and F1 scores, 0.9818 and 0.9812, respectively, and the lowest nice1 and nice2 error, 0.0115 and 0.0137, respectively, are obtained from DFCN. Nevertheless, the recall of 0.9806 obtained from DFCN is lower than that of 0.9968 obtained from the FRED-Net. For the UBIRIS.V2 database, the highest accuracy of 99.47% is obtained from DFCN. Moreover, the highest precision, 0.9592, and the lowest nice1 and nice2 error, 0.0052 and 0.0204 are obtained from DFCN. However, the recall and F1 scores of 0.9620 and 0.9606 obtained from DFCN are less than the values of 0.9852 and 0.9630 obtained from FRED-Net. Our results are similar to those of FRED-Net with the residual skip connection, which is also an excellent architecture. However, DFCN still has a competitive advantage,

TABLE 6. Comparison of DFCN with algorithms based on CNNs on the three iris databases.

Database	Approach	Acc(%)	P	R	F1	Nice1	Nice2
CASIA-Interval-V4	FCEDNs-Original [23]	94.39%	—	—	0.8826	0.0561	0.0588
	FCEDNs-Basic [23]	95.52%	—	—	0.9072	0.0448	0.0438
	FCEDNs-Bayesian-Basic [23]	96.09%	—	—	0.9192	0.0391	0.0407
	IrisDenseNet [43]	—	0.9810	0.9710	0.9758	—	—
	FRED-Net [45]	—	0.9659	**0.9910**	0.9783	—	—
	DFCN	**99.05%**	**0.9827**	0.9829	**0.9828**	**0.0094**	**0.0118**
IITD	FCEDNs-Original [23]	94.09%	—	—	0.8661	0.0591	0.0659
	FCEDNs-Basic [23]	94.61%	—	—	0.8892	0.0539	0.0594
	FCEDNs-Bayesian-Basic [23]	93.28%	—	—	0.8489	0.0682	0.0701
	IrisDensenet [43]	—	0.9716	0.9800	0.9756	—	—
	FRED-Net [45]	—	0.9253	**0.9968**	0.9569	—	—
	DFCN	**98.84%**	**0.9818**	0.9806	**0.9812**	**0.0115**	**0.0137**
UBIRIS.v2	FCEDNs-Original [23]	96.58%	—	—	0.7691	0.0342	0.1249
	FCEDNs-Basic [23]	95.57%	—	—	0.7700	0.0423	0.1517
	FCEDNs-Bayesian-Basic [23]	96.94%	—	—	0.8407	0.0306	0.1116
	HCNN [24]	98.89%	—	—	—	0.0111	—
	MCNN [24]	99.10%	—	—	—	0.0090	—
	FCDNN-original [42]	97.82%	0.8565	0.7429	0.7808	0.0218	—
	FCDNN-Segnet [42]	94.99%	0.5860	0.8541	0.6659	0.0501	—
	FCDNN-tuning [42]	99.30%	0.9488	0.9398	0.9390	0.0070	—
	FRED-Net [45]	—	0.9431	**0.9852**	**0.9630**	—	—
	DFCN	**99.47%**	**0.9592**	0.9620	0.9606	**0.0052**	**0.0204**

that we do not adopt any data augmentation method, unlike the other methods based on CNNs.

As mentioned above, the deeper architectures obtain better performance. However, the number of images in the adopted iris databases is small, and blindly adding convolutional layers for small databases leads to overfitting. As can be observed from TABLE 6, FCEDN-Original exhibits the worst performance and consists of 88 layers, which is far more than the other networks. Moreover, FCEDNs-Original consumes more computer resources and time. However, the shallower architectures, e.g., FCEDNs-Bayesian-Basic, cannot obtain more robust performance. The dense blocks adopted for DFCN effectively alleviate the overfitting and gradient vanishing. Moreover, DFCN balances the computational expense and robustness. Hence, the addition of convolutional layers to DFCN still obtains promising results.

C. THE COMPARISONS ON DIFFERENT GROUND-TRUTH MASKS

Comparative results on different ground-truth masks are given in this section. In contrast, we trained DFCN on the databases that contain only labeled iris regions, i.e., not only the iris regions but also the noise occluding the iris regions. We present the results in TABLE 7.

As TABLE 7 indicates, because noise characteristics, such as eyelashes, eyelids and light spots occlude the iris regions, which were not labeled, DFCN performs better on the public ground-truth masks. For the public ground-truth masks of CASIA-Interval-V4, the nice1 and nice2 error scores are 0.0094 and 0.0118, respectively, which are less than those of the proposed ground-truth masks in this paper with values of 0.0120 and 0.0148, respectively. In addition, the precision, recall and f1 score of the former are 0.9827, 0.9829 and 0.9828, respectively, which are greater than those of the proposed ground-truth masks with values of 0.9818, 0.9806 and 0.9812, respectively. Regarding the public ground-truth masks of IITD, the nice1 and nice2 error scores are 0.0115 and 0.0137, respectively, which are less than those of the proposed ground-truth masks in this paper with values of 0.0168 and 0.0184, respectively. Moreover, the precision, recall and f1 scores of the former are 0.9818, 0.9806 and 0.9812, respectively, which are greater than

TABLE 7. Comparison of different ground-truth masks.

Metric	The public ground-truth masks		The proposed ground-truth masks	
	CASIA-Interval-V4	IITD	CASIA-Interval-V4	IITD
Nice1	0.0094	0.0115	0.0120	0.0168
Nice2	0.0118	0.0137	0.0148	0.0184
P	0.9827	0.9818	0.9751	0.9685
R	0.9829	0.9806	0.9791	0.9774
F1	0.9828	0.9812	0.9771	0.9729

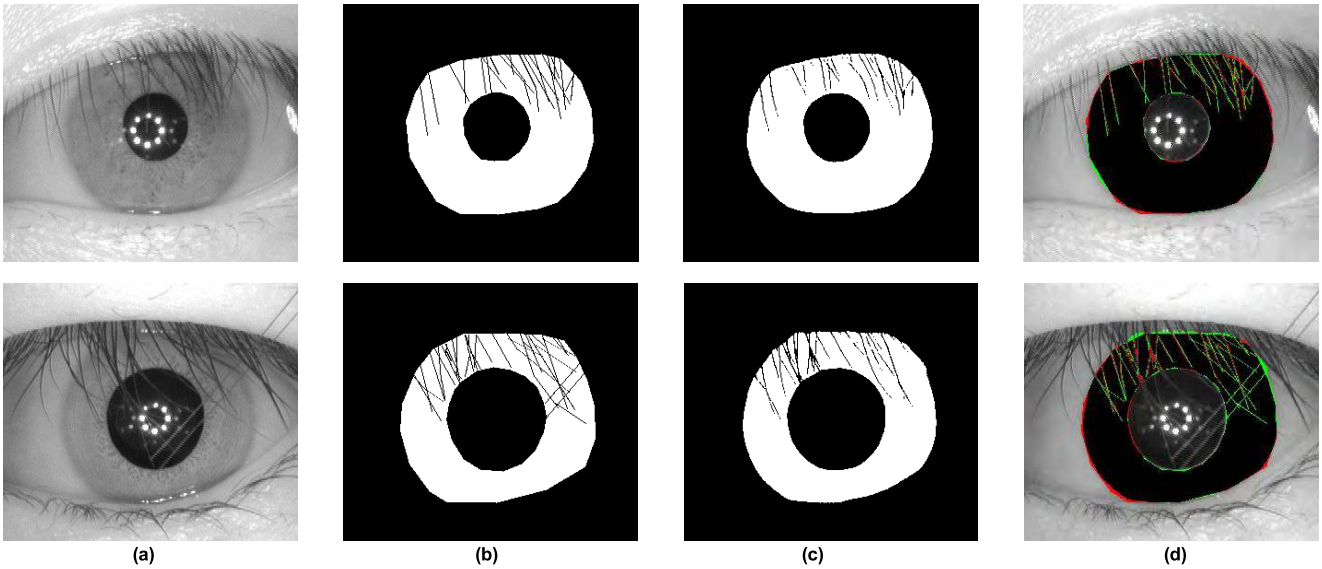

FIGURE 12. The segmentation results for the proposed CASIA-Interval-V4 ground-truth masks. (a) Iris images. (b) Ground-truth masks. (c) Predicted masks. (d) Segmentation results.

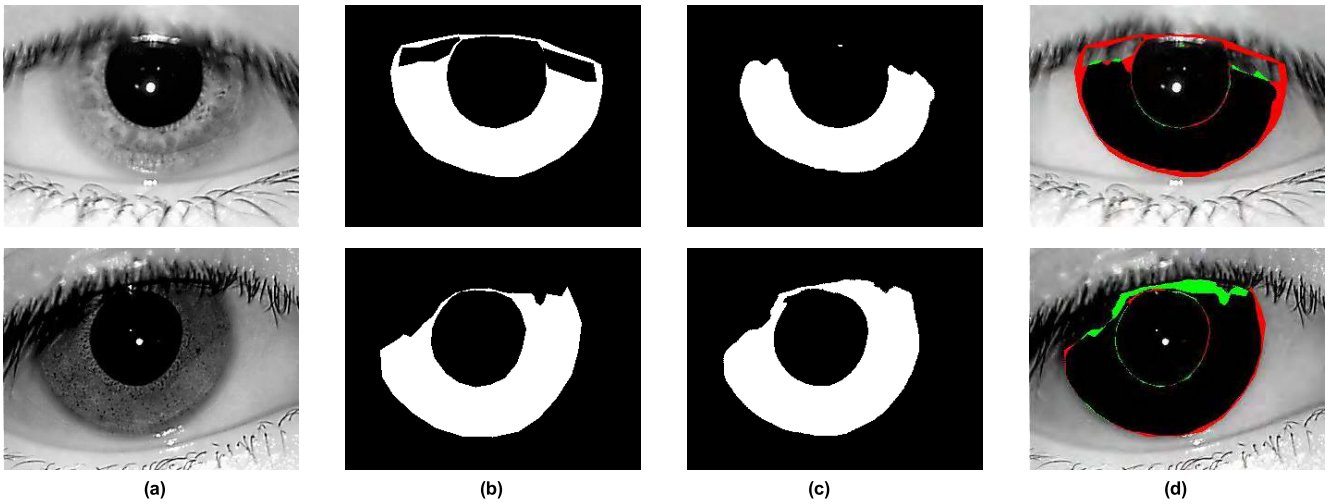

FIGURE 13. The segmentation results for the proposed IITD ground-truth masks. (a) Iris images. (b) Ground-truth masks. (d) Segmentation results.

those of the latter, 0.9685, 0.9774 and 0.9729, respectively. FIGURE 12 and FIGURE 13 demonstrate the performance of DFCN for the proposed ground-truth masks.

As shown in FIGURE 12 and FIGURE 13, the 4 columns represent the iris images, the corresponding ground-truth masks, the prediction masks and the segmentation result images (the false positive and negative errors are presented as green and red, and the true positive case is shown as black). The noise regions cannot be effectively recognized, especially on the images from the IITD iris database. Based on our overall analysis, we suggest some possible reasons: On the one hand, it is more difficult to recognize our proposed

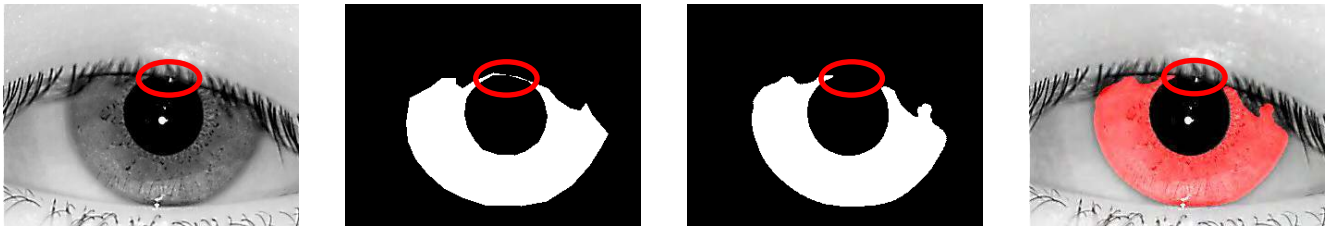

FIGURE 14. The segmentation results for the proposed IITD ground-truth masks. (a) Iris images. (b) Ground-truth masks. (c) Predict masks. (d) Segmentation results.

ground-truth masks. On the other hand, during labeling the databases using Labelme, the lines that labeled the eyelashes are not coincident with the true regions of the eyelashes. Above all, in the IITD iris database, the eyelashes of iris images are thick and severely occlude the iris regions. In other words, the iris pixels are labeled as non-iris pixels, which lead to a misclassification of the iris pixels to the eyelash pixels. Nonetheless, the features learned by DFCN are robust, as shown in FIGURE 14. The 4 columns of FIGURE 14 present an iris image of the IITD iris database, the corresponding proposed ground-truth masks, the corresponding prediction masks and the added images of the prediction masks and iris images (the white pixels of prediction masks are labeled red). The area marked by the red circle in the iris images does not belong to the iris, which is labeled as iris pixels in the ground-truth masks, yet it is classified as non-iris pixels in the prediction masks. In other words, although DFCN cannot recognize all noise occluding the iris regions, the shape of the noise recognized is more similar to the real shape, which demonstrates the effectiveness and robustness of DFCN.

VI. CONCLUSION

Iris segmentation algorithms play an important role in iris recognition systems and directly affect the accuracy of iris verification and recognition. We proposed an iris segmentation architecture based on CNNs combined with dense blocks, referred to as DFCN. The encoder of DFCN consists of dense blocks, and the decoder of DFCN obtains the output prediction masks via transpose convolution. To evaluate the performance of DFCN, we adopted three public iris databases captured under different conditions, namely, CASIA-Interval-V4, IITD and UBIRIS.v2, with the corresponding ground-truth masks. Moreover, we labeled the eyelash regions occluding the iris regions of the CASIA-Interval-V4 and IITD iris databases using the Labelme software package, which is also used for training and testing. To reflect the superiority of DFCN in terns of many aspects, we adopted a variety of metrics used for evaluating the iris segmentation algorithms, i.e., the accuracy, precision, recall, f1 score, and nice1 and nice2 error scores. In addition, we compared some conventional and CNN-based iris segmentation algorithms. The results of the experiments reveal that the iris segmentation architecture proposed in this paper outperforms most of the other algorithms, which demonstrates its superiority and robustness. Nevertheless, the performance of DFCN on the public ground-truth masks is better than that on our labeled ground-truth masks; this finding is related to the adopted public iris databases and the method of labeling. Thus, more attention is needed in the future for the design of more robust iris segmentation algorithms for iris databases under nonideal conditions and for more effective ways of labeling.

ACKNOWLEDGMENT

The research in this paper uses the CASIA databases provided by the Institute of Automation, Chinese Academy of Science; IITD iris image database provided by IIT Delhi, New Delhi, India; UBIRIS.V2 iris database provided by the Department of Computer Science, University of Beira Interior; and Irisseg-ep database provided by WaveLab of the University of Salzburg.

REFERENCES

[1] R. Jillela and A. A. Ross, *Methods for Iris Segmentation*. London, U.K.: Springer, 2013, pp. 239–279.
[2] H. Hofbauer, F. Alonso-Fernandez, J. Bigun, and A. Uhl, "Experimental analysis regarding the influence of iris segmentation on the recognition rate," *IET Biometrics*, vol. 5, no. 3, pp. 200–211, 2015.
[3] A. Szczepa ski, K. Misztal, and K. Saeed, "Pupil and iris detection algorithm for near-infrared capture devices," in *Proc. IFIP Int. Conf. Comput. Inf. Syst. Ind. Manage.* Berlin, Germany: Springer, 2014, pp. 141–150.
[4] K. Okokpujie, E. Noma-Osaghae, S. John, and A. Ajulibe, "An improved iris segmentation technique using circular hough transform," in *Proc. Int. Conf. Inf. Theoretic Secur.*, 2017, pp. 203–211.
[5] S. Umer and B. C. Dhara, "A fast iris localization using inversion transform and restricted circular Hough transform," in *Proc. 8th Int. Conf. Adv. Pattern Recognit.*, Jan. 2015, pp. 1–6.
[6] S. Barra, C. Bisogni, M. Nappi, and S. Ricciardi, "F-FID: Fast fuzzy-based iris de-noising for mobile security applications," in *Multimedia Tools and Applications*. 2019, pp. 1–21.
[7] D. A. Roy and U. S. Soni, "IRIS segmentation using Daughman's method," in *Proc. Int. Conf. Elect., Electron., Optim. Techn. (ICEEOT)*, Mar. 2016, pp. 2668–2676.
[8] Y. Hu, K. Sirlantzis, and G. Howells, "Improving colour iris segmentation using a model selection technique," *Pattern Recognit. Lett.*, vol. 57, pp. 24–32, May 2015.
[9] Z. Zhao and A. Kumar, "An accurate iris segmentation framework under relaxed imaging constraints using total variation model," in *Proc. IEEE Int. Conf. Comput. Vis.*, Dec. 2015, pp. 3828–3836.
[10] A. Uhl and P. Wild, "Weighted adaptive Hough and ellipsopolar transforms for real-time iris segmentation," in *Proc. 5th IAPR Int. Conf. Biometrics*, 2012, pp. 283–290.
[11] A. Radman, K. Jumari, and N. Zainal, "Fast and reliable iris segmentation algorithm," *IET Image Process.*, vol. 7, no. 1, pp. 42–49, Feb. 2013.

[12] S. A. Sahmoud and I. S. Abuhaiba, "Efficient iris segmentation method in unconstrained environments," *Pattern Recognit.*, vol. 46, no. 12, pp. 3174–3185, 2013.
[13] A. Radman, K. Jumari, and N. Zainal, "Iris segmentation in visible wavelength images using circular gabor filters and optimization," *Arabian J. Sci. Eng.*, vol. 39, no. 4, pp. 3039–3049, 2014.
[14] A. Radman, N. Zainal, and S. A. Suandi, "Automated segmentation of iris images acquired in an unconstrained environment using HOG-SVM and GrowCut," *Digit. Signal Process.*, vol. 64, pp. 60–70, May 2017.
[15] C. Szegedy *et al.*, "Going deeper with convolutions," in *Proc. IEEE Conf. Comput. Vis. Pattern Recognit.*, Jun. 2015, pp. 1–9.
[16] K. He, X. Zhang, S. Ren, and J. Sun, "Deep residual learning for image recognition," in *Proc. IEEE Conf. Comput. Vis. Pattern Recognit.*, Jun. 2016, pp. 770–778.
[17] E. Shelhamer, J. Long, and T. Darrell, "Fully convolutional networks for semantic segmentation," *IEEE Trans. Pattern Anal. Mach. Intell.*, vol. 39, no. 4, pp. 640–651, Apr. 2017.
[18] V. Badrinarayanan, A. Kendall, and R. Cipolla, "SegNet: A deep convolutional encoder-decoder architecture for image segmentation," *IEEE Trans. Pattern Anal. Mach. Intell.*, vol. 39, no. 12, pp. 2481–2495, Dec. 2017.
[19] O. Ronneberger, P. Fischer, and T. Brox, "U-Net: Convolutional networks for biomedical image segmentation," in *Proc. Int. Conf. Med. Image Comput. Comput.-Assist. Intervent.*, 2015, pp. 234–241.
[20] F. Marra, G. Poggi, C. Sansone, and L. Verdoliva, "A deep learning approach for iris sensor model identification," *Pattern Recognit. Lett.*, vol. 113, pp. 46–53, Oct. 2018. doi: 10.1016/j.patrec.2017.04.010.
[21] E. Ribeiro, A. Uhl, F. Alonso-Fernandez, and R. A. Farrugia, "Exploring deep learning image super-resolution for iris recognition," in *Proc. 25th Eur. Signal Process. Conf.*, 2017, pp. 2176–2180.
[22] A. S. Al-Waisy, R. Qahwaji, S. Ipson, S. Al-Fahdawi, and T. A. M. Nagem, "A multi-biometric iris recognition system based on a deep learning approach," *Pattern Anal. Appl.*, vol. 21, no. 3, pp. 783–802, 2017.
[23] E. Jalilian, A. Uhl, "Iris segmentation using fully convolutional encoder-decoder networks," in *Deep Learning for Biometrics*. 2017, pp. 133–155.
[24] N. Liu, H. Li, M. Zhang, J. Liu, Z. Sun, and T. Tan, "Accurate iris segmentation in non-cooperative environments using fully convolutional networks," in *Proc. Int. Conf. Biometrics*, 2016, pp. 1–8.
[25] G. Huang, Z. Liu, L. van der Maaten, and K. Q. Weinberger, "Densely connected convolutional networks," in *Proc. CVPR*, Jul. 2017, pp. 4700–4708.
[26] *Chinese Academy of Science—Institute of Automation, CASIA-IRIS-V4 Iris Image Database Version4.0 (CASIA-IRIS-V4-IrisV4)*. Accessed: Dec. 10, 2018. [Online]. Available: http://biometrics.idealtest.org/dbDetailForUser.do?id=4
[27] A. Kumar and A. Passi, "Comparison and combination of iris matchers for reliable personal authentication," *Pattern Recognit.*, vol. 43, no. 3, pp. 1016–1026, 2010. [Online]. Available: http://www4.comp.polyu.edu.hk/~csajaykr/IITD/Database_Iris.html
[28] *Labelme*. Accessed: Dec. 20, 2018. [Online]. Available: https://github.com/wkentaro/labelme
[29] D. P. Kingma, J. Ba, "Adam: A method for stochastic optimization," *Computer Science*, 2014.
[30] H. Hofbauer, F. Alonso-Fernandez, P. Wild, J. Bigun, and A. Uhl, "A ground truth for iris segmentation," in *Proc. 22nd Int. Conf. Pattern Recognit.*, 2014, pp. 527–532.
[31] H. Proenca, S. Filipe, R. Santos, J. Oliveira, and L. A. Alexandre, "The UBIRIS.v2: A database of visible wavelength iris images captured on-the-move and at-a-distance," *IEEE Trans. Pattern Anal. Mach. Intell.*, vol. 32, no. 8, pp. 1529–1535, Aug. 2010.
[32] S. Umer, B. C. Dhara, and B. Chanda, "Texture code matrix-based multi-instance iris recognition," *Pattern Anal. Appl.*, vol. 19, no. 1, pp. 283–295, 2016.
[33] P. Wild, H. Hofbauer, J. Ferryman, and A. Uhl, "Segmentation-level fusion for iris recognition," in *Proc. Int. Conf. Biometrics Special Interest Group*, 2015, pp. 1–6.
[34] T. Tan, Z. He , Z. Sun, "Efficient and robust segmentation of noisy iris images for non-cooperative iris recognition," *Image Vis. Comput.*, vol. 28, no. 2, pp. 223–230, 2010.
[35] A. Gangwar, A. Joshi, A. Singh, F. Alonso-Fernandez, and J. Bigun, "IrisSeg: A fast and robust iris segmentation framework for non-ideal iris images," in *Proc. Int. Conf. Biometrics*, 2016, pp. 1–8.
[36] F. Alonso-Fernandez and J. Bigun, "Iris boundaries segmentation using the generalized structure tensor. A study on the effects of image degradation," in *Proc. IEEE 5th Int. Conf. Biometrics, Theory, Appl. Syst.*, Sep. 2012, pp. 426–431.
[37] C. Rathgeb, A. Uhl, and P. Wild, *Iris Biometrics: From Segmentation to Template Security*. Berlin, Germany: Springer, 2012.
[38] G. Sutra, B. Dorizzi, S. Garcia-Salicetti, N. Othman. (2012). *A Biometric Reference System for Iris, Osiris Version 4.1*. [Online]. Available: http://svnext.it-sudparis.eu/svnview2-eph/ref_syst/Iris_Osiris_v4.1/
[39] A. Uhl and P. Wild, "Multi-stage visible wavelength and near infrared iris segmentation framework," in *Proc. Int. Conf. Image Anal. Recognit.*, 2012, pp. 1–10.
[40] *Masek*. Accessed: Dec. 18, 2018. [Online]. Available: http://www.peterkovesi.com/studentprojects/libor/sourcecode.html
[41] N. Susitha and R. Subban, "Reliable pupil detection and iris segmentation algorithm based on SPS," *Cogn. Syst. Res.*, to be published.
[42] B. Shabab, S. Thavalengal, and P. Corcoran, "An end to end deep neural network for iris segmentation in unconstrained scenarios," *Neural Netw.*, vol. 16, pp. 79–95, Oct. 2018.
[43] M. Arsalan, R. A. Naqvi, D. S. Kim, P. H. Nguyen, M. Owais, and K. R. Park, "IrisDenseNet: Robust iris segmentation using densely connected fully convolutional networks in the images by visible light and near-infrared light camera sensors," *Sensors*, vol. 18, no. 5, pp. 1501–1531, 2018.
[44] M. Arsalan, D. S. Kim, M. B. Lee, M. Owais, and K. R. Park, "FRED-Net: Fully residual encoder–decoder network for accurate iris segmentation," *Expert Syst. Appl.*, vol. 122, pp. 217–241, May 2019.
[45] *Tensorflow*. Accessed: Oct. 18, 2016. [Online]. Available: https://www.tensorflow.org/

YING CHEN was born in 1981. He received the B.E., master's, and Ph.D. degrees from Jilin University, Changchun, Jilin, China. He is currently an Associate Professor with Nanchang Hangkong University, Nanchang, Jiangxi, China. His current research interests include wireless sensor networks, the Internet of Things, biometric information recognition, and information security.

WENYUAN WANG was born in 1996. He received the B.S. degree in software engineering from Nanchang Hangkong University, Nanchang, Jiangxi, China, where he is currently pursuing the M.S. degree under the supervision of Prof. Y. Chen. His current research interests include deep learning and iris recognition.

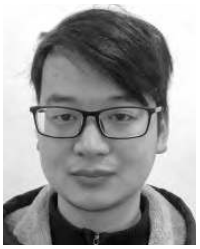

ZHUANG ZENG was born in 1995. He received the B.S. degree in computer science and technology from Hubei Engineering University, Xiaogan, Hubei, China. He is currently pursuing the M.S. degree with Nanchang Hangkong University under the supervision of Prof. Y. Chen. His current research interests include deep learning and biometric information recognition.

YERONG WANG was born in 1993. He received the B.S. degree in software engineering from the Changchun Institute of Technology, Changchun, Jilin, China. He is currently pursuing the M.S. degree with Nanchang Hangkong University, under the supervision of Prof. Y. Chen. His current research interests include software engineering and image processing.